CHAPTER 6

TITANIUM SUBSTITUTED Y-TYPE BARIUM HEXAFERRITE (CO_2-Y); AS A PHOTOCATALYST FOR THE TREATMENT OF METHYL ORANGE CONTAMINATED WASTEWATER

6.1 Introduction

The Ti-substituted Y-type barium hexaferrite $Ba_2Co_2Fe_{12-x}Ti_xO_{22}$ (x = 0.0, 0.1, 0.2, 0.3, 0.4 & 0.5) are synthesized using the nitrate-based sol-gel auto combustion method and investigated their photocatalytic efficiency within the decomposition of non-biodegradable organic dye (methyl orange) from wastewater, one of the significant water contaminants. The proposed hexaferrite samples are prepared using the analytical grades of barium nitrate [$Ba(NO_3)_2$], cobalt nitrate [$Co(NO_3)_3.6H_2O$], ferrous nitrate [$Fe(NO_3)_3.9H_2O$], titanium nitrate [$Ti(N0_3)_4.4H_20$] as elemental precursors and citric acid [$C_6H_8O_7 \cdot H_2O$] as a chelating agent or fuel within the process.

To overcome the major issues (poor thermo-chemical stability, low degradation rate, and incomplete removal) related to the largely utilized spinel-based ferrite and few hexaferrite (M-type) systems, the $Ba_2Co_2Fe_{12}O_{22}$ ferrites are exploited with several advantages likewise better thermochemical stability, excellent mechanical hardness, low band gap energy, wear and corrosion resistance, higher value of Curie temperature, magnetic recycling, and redox characteristics for the exploration of their suitability within this field [(Jotania and Virk, 2012), (Tasca *et al.*, 2012), (Dhakshinamoorthy, Alvaro and Garcia, 2011), (Valero-Luna, Palomares-Sanchéz, and Ruíz, 2016), (Farghali, Khedr, and Moustafa, 2008), (Alrebdi *et al.*, 2022)].

The selection of titanium as a substituting element is inspired by earlier studied ferrite systems, where the replacement of titanium ions at the iron site results in a low bandgap energy value [(Kumar and Kar, 2014), (Rajivgandhi *et al.*, 2021)]. The capability to absorb the solar spectrum is determined by the bandgap (E_g) value of the ferrite being utilized as a photocatalyst. A narrow energy gap between the valance and conduction band may provide a wider absorption of the solar spectrum; hence it can use the visible light more efficiently [(Yan *et al.*, 2013)].

The photocatalytic degradation efficiency of the hexaferrite samples is evaluated by the degradation of methyl orange (MO). To examine the degradation efficiency, 0.1 mg of the dried hexaferrite sample is added to the 2 ml of aqueous MO solution (concentration 4.6 ppm) within a quartz cuvette (capacity of 4 ml) with a 1 cm of path span. The pH level of this suspension is tuned at 3 by the dropwise addition of 0.1 M HCl. The admixture is allowed to be stirred continuously for the next 15 minutes (in the dark condition) to achieve the equilibrium condition for adsorption-desorption. Later, 100 μL of 1.4 M hydrogen peroxide (H_2O_2) is introduced to it. Two protocols are implemented in the next step with two identical sets of the above-mentioned reaction mixture. The UV-visible spectrum for the reaction mixture is allowed to be measured within an equal interval of 10 minutes for both Fenton (in dark conditions) and photo-Fenton (in the presence of a visible light source, a cool white LED emitting an irradiance of 930 watts/m^2). Furthermore, the photocatalytic degradation performance of pristine and titanium substituted sample, having the lowest bandgap, is quantified and compared in terms of apparent rate constant (K_{arc}) value and turnover frequency values. The enriched photocatalytic performance is correlated with the existence of multi-valance states for transition metal cations and the availability of oxygen vacancy, which is confirmed by the surface chemistry using the XPS analysis.

6.2 Results and discussion

The XRD pattern for the calcined powder of titanium substituted Co_2-Y is shown in Fig. 6.1(a). The presence of sharp characteristic peaks corresponding to the $Ba_2Co_2Fe_{12}O_{22}$ (standard JCPDS card no 440206) within the obtained pattern confirms the formation of high purity Y-type barium hexaferrite (Co_2-Y) phase along with good crystallinity. Furthermore, several structural parameters such as average crystallite size, lattice

parameters, *c/a* ratio, unit cell volume, X-ray density, and lattice strain are calculated and tabulated in Table 6.1.

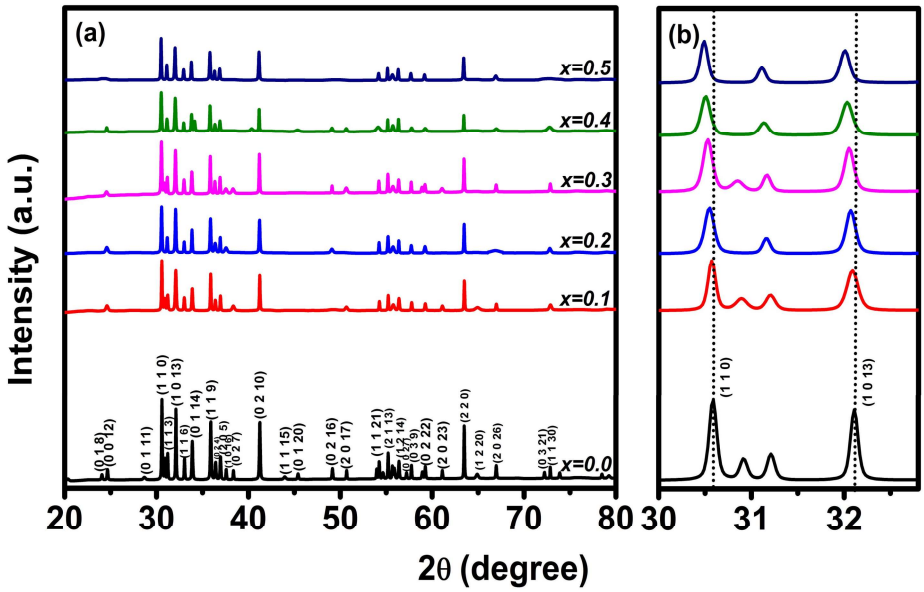

Figure 6.1 XRD patterns of calcined $Ba_2Co_2Fe_{12-x}Ti_xO_{22}$ (x = 0.0, 0.1, 0.2, 0.3, 0.4 & 0.5) ferrite powders.

The XRD pattern confirms the successful substitution of Ti^{4+} at the Fe^{3+} site. It is found that the crystallite size is in the range of 64-72 nm. The XRD results agree with the substitution of a larger cation Ti^{4+} (0.68 Å) at the site of a smaller cation Fe^{3+} (0.64 Å) by increasing the value of the lattice parameters along with the unit cell volume [(Jia *et al.*, 2013)]. A peak shifting (Fig. 6.1(b)) is observed towards the left side. The crystal axis ratio (*c/a*) is found to be 7.429 for x = 0.0 and 7.421 for x = 0.5, which lies within the permissible range for the formation of the Co_2-Y phase [(Suthar *et al.*, 2020)]. The X-ray densities follow the decreasing trend with substitution. It is in good agreement with both the decreasing molecular weight and the increasing unit cell volume. The crystallite distortions that arise while substituting a larger cation at the smaller cation site are quantified using the determination of lattice strain using the Williamson-Hall method, as depicted in Fig.

6.2. The lattice strain is found to be positive (volumetric expansion within the unit cell) for all these samples, which keeps rising continuously with increasing Ti^{4+} ions substitution.

Table 6.1 Crystallite size, lattice constants (*a* & *c*), (*c*/*a*) ratio, unit cell volume, X-ray density and lattice strain of the calcined $Ba_2Co_2Fe_{12-x}Ti_xO_{22}$ (x = 0.0, 0.1, 0.2, 0.3, 0.4 & 0.5) ferrite powders.

Composition	Crystallite size (nm)	Lattice parameters		Axial ratio	Unit cell volume	X-ray density	Lattice strain
		a (Å)	*c* (Å)	(*c*/*a*)	($Å^3$)	(g/cm^3)	(ε)
x = 0.0	72.27	5.844	43.417	7.429	1284.314	5.266	6.75×10^{-4}
x = 0.1	69.07	5.845	43.411	7.426	1284.608	5.262	8.95×10^{-4}
x = 0.2	67.17	5.852	43.459	7.426	1289.114	5.240	3.85×10^{-3}
x = 0.3	64.19	5.853	43.463	7.426	1289.444	5.236	4.27×10^{-3}
x = 0.4	64.09	5.861	43.511	7.424	1294.222	5.213	5.34×10^{-3}
x = 0.5	64.01	5.864	43.515	7.421	1295.826	5.204	5.62×10^{-3}

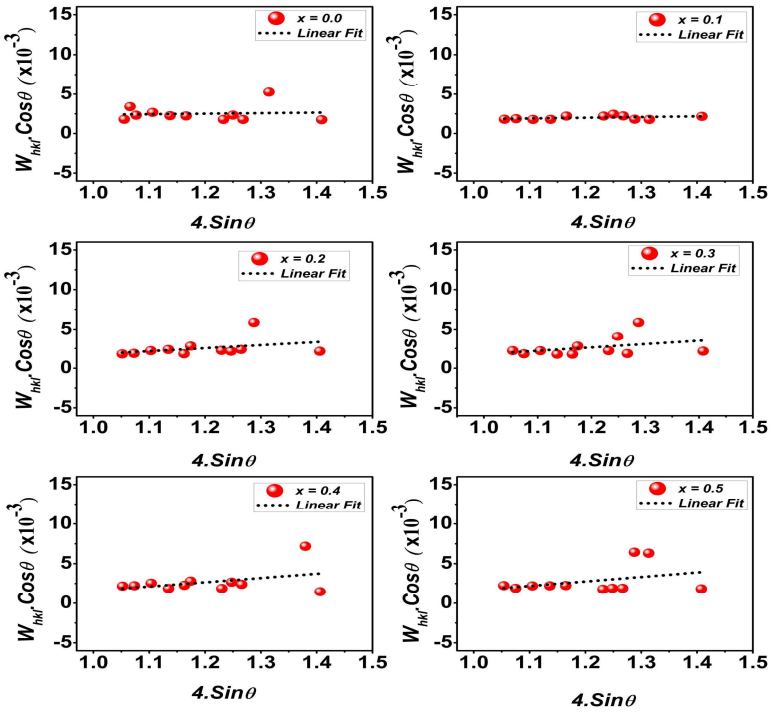

Figure 6.2 Williamson–Hall plot for calcined $Ba_2Co_2Fe_{12-x}Ti_xO_{22}$ (x = 0.0, 0.1, 0.2, 0.3, 0.4 & 0.5) ferrite powders.

The structural variations within the titanium substituted Y-type barium hexaferrite (Co_2-Y) are analyzed further using FTIR spectra by confirming the presence of various characteristic bands corresponding to their specific absorption peak positions. In Fig. 6.3, the FTIR spectra for undoped (x = 0.0) calcined powder consists of two major absorption peaks, one at 400.15 cm^{-1} (corresponding to asymmetric stretching of metal cation at the octahedral site) and the second at 584.32 cm^{-1} (corresponding to asymmetric stretching of metal cation at the tetrahedral site). It is considered the characteristic peaks for the cationic vibrations within the spinel block of the Co_2-Y structure [(Adeela *et al.*, 2016)].

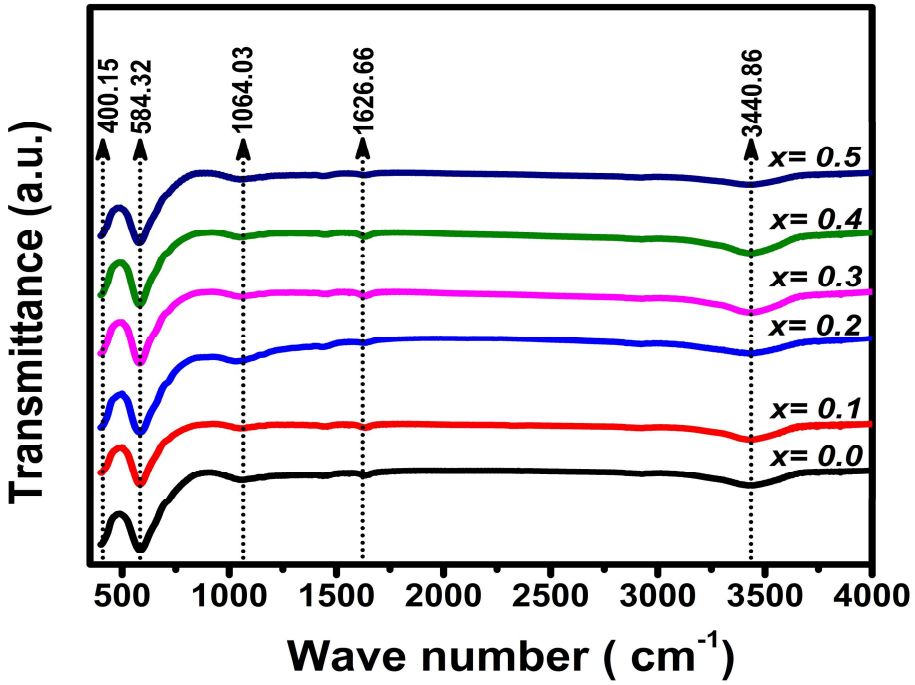

Figure 6.3 FT-IR spectra of calcined $Ba_2Co_2Fe_{12-x}Ti_xO_{22}$ (x = 0.0, 0.1, 0.2, 0.3, 0.4 & 0.5) ferrite powders.

The substitution of Ti^{4+} ions at the Fe^{3+} site allows a slight shifting of these characteristic bands towards the higher wavenumber with increasing concentration. The force constants associated with the Fe-O bonds and respective bond length values are calculated and tabulated in Table 6.2. The results show that the Fe-O bond length is

increased with the substitution of Ti^{4+} within the hexaferrite (Co_2-Y). The bond length variation can be correlated due to the ionic radius mismatch (introducing a larger cation at a smaller cation site), which also favors the volumetric expansion suggested by XRD studies. Apart from these two characteristic peaks, the co-existence of a few minor absorption peaks within the range of 1064.03 cm^{-1} to 1626.66 cm^{-1} is also observed. It may be attributed due to the presence of metal-oxygen-metal bonding likewise Fe-O-Fe or Co-O-Co (between 1100 to 1500 cm^{-1}), or the presence of residual traces of N–O stretching vibration (between 1475 and 1550 cm-1), or N–H band (between 1600–1640 cm-1). It may be associated with using ammonia solution while adjusting the pH. The peaks around 1626 cm-1 and 3440 cm-1 may be attributed to the O-H stretching vibrations due to the adsorbed moisture content at the surface [(Adeela *et al.*, 2016), (Lalegani and Nemati, 2015)].

Table 6.2 Characteristic wave number, effective mass for Fe-O bond, force constant, and corresponding bond length of the calcined $Ba_2Co_2Fe_{12-x}Ti_xO_{22}$ (x = 0.0, 0.1, 0.2, 0.3, 0.4 & 0.5) ferrite powders.

Composition	Wave number (cm^{-1})	Effective mass (10^{-26} kg)	Force constant (N/cm)	Bond length (Fe–O) (Å)
x = 0.0	584.3255	2.0648	2.5039	1.8935
x = 0.1	582.8792	2.0648	2.4915	1.8966
x = 0.2	582.3970	2.0648	2.4874	1.8977
x = 0.3	581.4328	2.0648	2.4792	1.8998
x = 0.4	580.9507	2.0648	2.4751	1.9008
x = 0.5	579.9865	2.0648	2.4669	1.9029

All the calcined hexaferrite samples dispersed within the isopropyl alcohol (IPA) are analyzed for their average particle size (APS) along with poly-dispersion index (PdI), using the dynamic light scattering-based technique (shown in Fig. 6.4). The results suggest that

particle sizes are found to be in decreasing order (from 1.835 µm for x = 0.0 to 1.055 µm for x = 0.5) with Ti^{4+} substitution within the Co_2-Y hexaferrite. The particle size distribution quality can be explained by PdI value, which indicates the non-uniformity of the powder sample on a scale of 0 to 1 [(Danaei *et al.*, 2018)]. The results suggest that all these samples consist of a wide range of size distribution owing to their platelet-like shape and the substitution of Ti^{4+} leads to the lower PdI value.

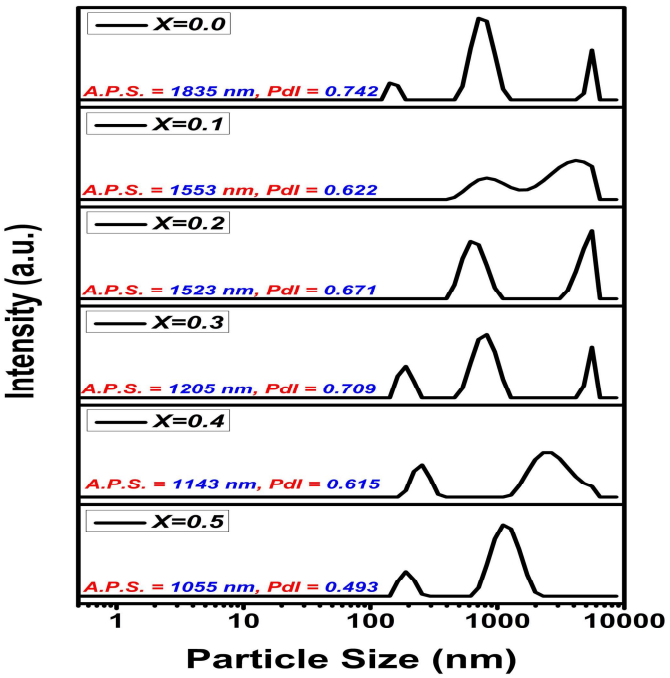

Figure 6.4 DLS analysis for particle size distribution of $Ba_2Co_2Fe_{12-x}Ti_xO_{22}$ (x = 0.0, 0.1, 0.2, 0.3, 0.4 & 0.5) ferrite powders.

To investigate the influence of Ti^{4+} ions substitution on the magnetic properties of Y-type barium hexaferrite (Co_2-Y), the magnetization curves are recorded at 300 K (shown in Fig. 6.5) at a maximum applied field of ± 6 Tesla. The results suggest the ferrimagnetic behavior in all synthesized samples. The sample doesn't achieve saturation within the applied magnetic field range; the exact saturation magnetization value is estimated at the high-field regime using the Stoner–Wohlfarth law of approach (shown in Fig. 6.6).

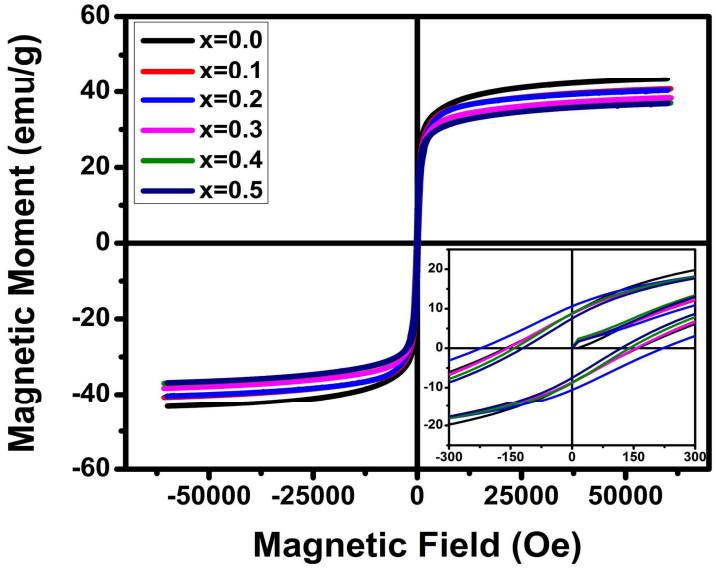

Figure 6.5 Magnetic hysteresis loops of calcined $Ba_2Co_2Fe_{12-x}Ti_xO_{22}$ (x = 0.0, 0.1, 0.2, 0.3, 0.4 & 0.5) ferrite powders.

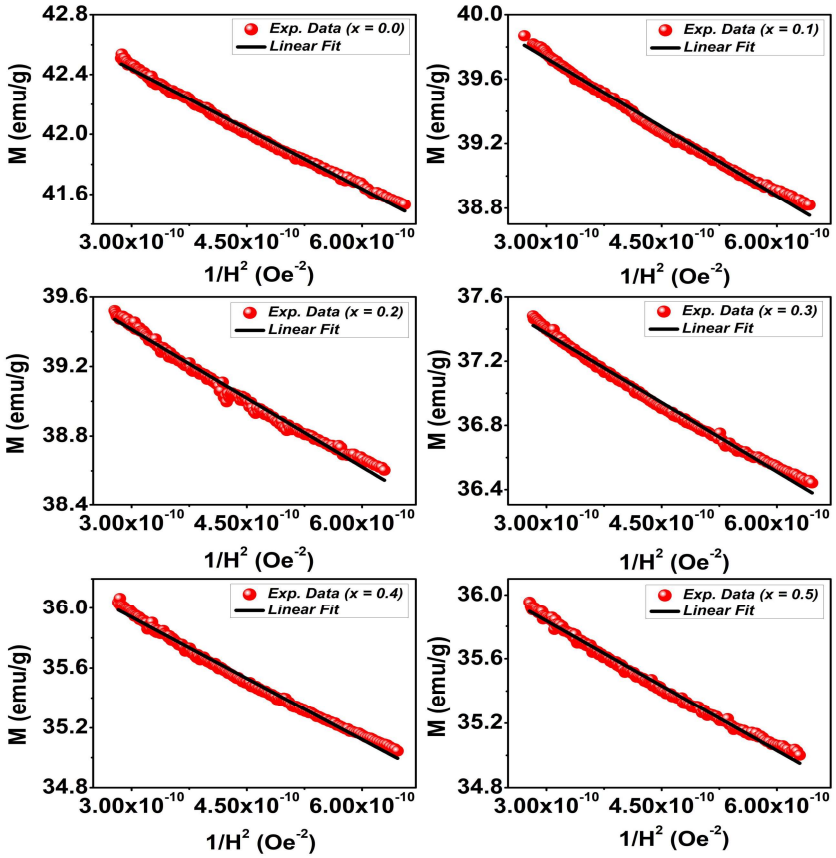

Figure 6.6 *M* vs. H^{-2} plot (Stoner–Wohlfarth model) of calcined $Ba_2Co_2Fe_{12-x}Ti_xO_{22}$ (x = 0.0, 0.1, 0.2, 0.3, 0.4 & 0.5) ferrite powders.

To evaluate the variation of temperature-dependent magnetization properties with Ti^{4+} ion substitution, thermomagnetic curves (ZFC and FC) are obtained within the temperature range of 300 to 900 K at an applied field of 300 Oe, as shown in Fig. 6.7. The Curie temperature (Tc) (Inserted fig) is measured at the minima from the temperature-dependent first-order derivative (*dM/dT*) curve.

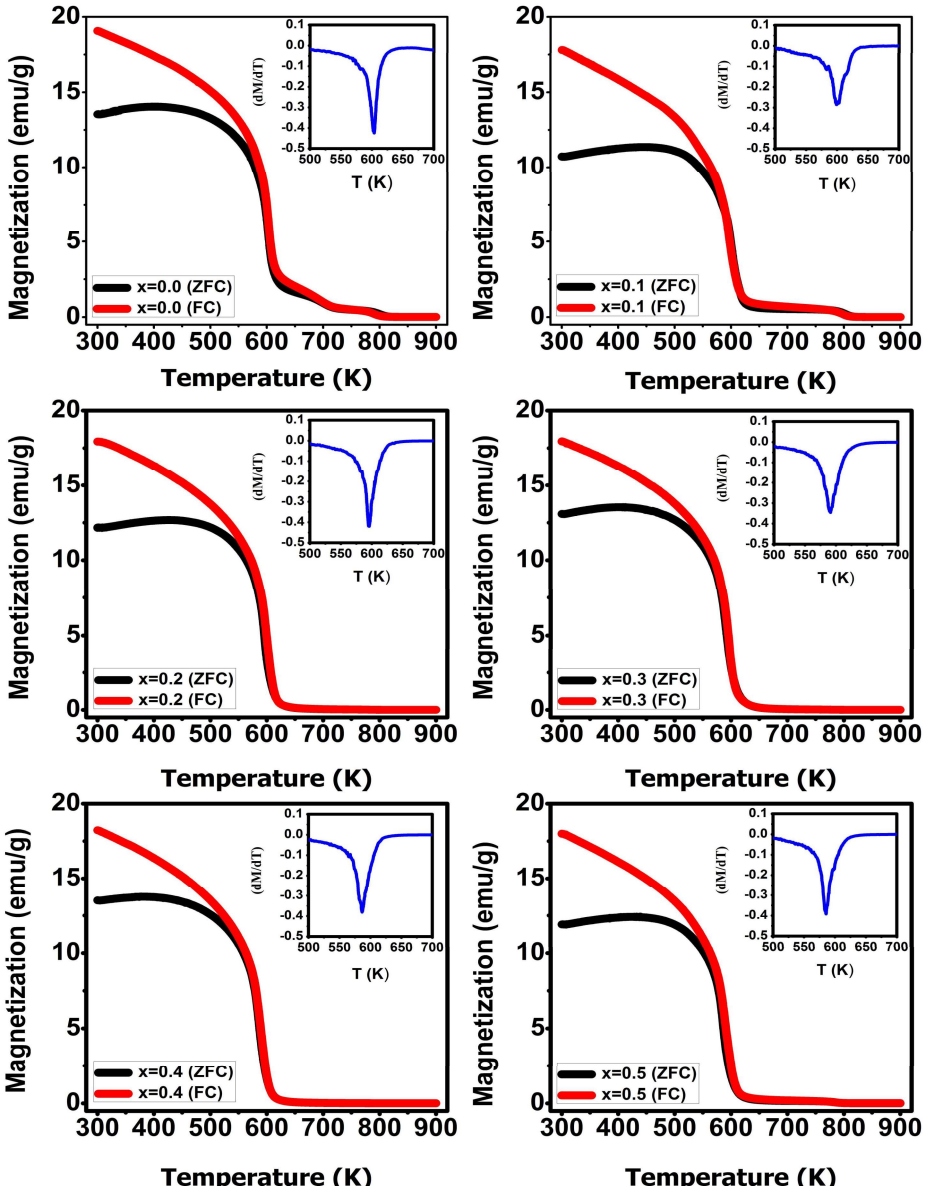

Figure 6.7 Magnetization along and its first order derivative (*dM/dT*) as a function of temperature (K) for calcined $Ba_2Co_2Fe_{12-x}Ti_xO_{22}$ (x = 0.0, 0.1, 0.2, 0.3, 0.4 & 0.5) ferrite powders.

All the derived parameters such as saturation magnetization (M_s), coercivity field (H_c), remnant magnetization (M_r), number of Bohr magneton (N_{BM}), squareness ratio (M_r/M_s), magnetic anisotropy constant (K_1), Curie temperature (Tc) are calculated and tabulated in Table 6.3.

Table 6.3 Saturation magnetization (M_s), number of Bohr magneton, coercivity (H_c), magnetic retentivity (M_r),), squareness ratio, magnetic anisotropy constant (K_1), and Curie Temperature (Tc) of the calcined $Ba_2Co_2Fe_{12-x}Ti_xO_{22}$ (x = 0.0, 0.1, 0.2, 0.3, 0.4 & 0.5) ferrite powders.

Composition	M_s (emu/g)	Bohr magneton (N_{BM})	Hc (Oe)	M_r	(M_r/M_s)	K_1 (HA^2/Kg)	Curie Temperature (K)
x = 0.0	43.39	10.55	160.84	8.78	0.2023	3.49×10^{-1}	603.76
x = 0.1	40.73	9.89	156.05	8.74	0.2145	3.18×10^{-1}	599.09
x = 0.2	40.42	9.81	222.24	10.6	0.2622	4.49×10^{-1}	595.84
x = 0.3	38.35	9.31	155.48	8.66	0.2258	2.98×10^{-1}	591.19
x = 0.4	36.95	8.96	139.25	8.83	0.2389	2.57×10^{-1}	586.52
x = 0.5	36.81	8.92	120.66	7.54	0.2048	2.22×10^{-1}	585.71

The results suggest that the value of saturation magnetization (M_s) along with the number of Bohr magneton (N_{BM}) is found to be decreased with the substitution of titanium ions within the hexaferrite. This decreasing behavior can be explained by the replacement of a magnetic (Fe^{3+}) ion with a nonmagnetic (Ti^{4+}) ion within a hexaferrite system [(Kumar, Kumar, and Ghumman, 2017)]. The coercivity values are found to be increased linearly up to the x = 0.2 and achieved their maximum value of 222.24 Oe. The improvement of the coercive field may be due to the enhanced value of lattice imperfections with nonmagnetic inclusion within the system, generation of Fe^{2+}-Ti^{4+} pair by replacement of two Fe^{3+} ions,

having larger magneto-crystalline anisotropy, larger ionic radius, and enhanced lattice strain value [(Ounnunkad, 2006), (Kumar *et al.*, 2018), (Rao *et al.*, 2009)]. Further increment of Ti^{4+} content allows for a decrease of coercive field. It can be explained by lowering the anisotropy constant value or decreasing the average particle size value along with the dominance of single-domain particles (nearly 1.18 μm) [(Kumar *et al.*, 2018), (Hosseinkhan Nejad, Farzin and Heydari, 2017), (Park *et al.*, 2015)]. The retentivity value (magnetization holding capability after removal of the externally applied field) shows a random behavior with substituting Ti^{4+} ions. This random behavior can be explained by the ferroxplana nature of Co_2-Y hexaferrite, where the preferred plane of magnetization is found to be within its basal plane or in a right circular cone at an angle to the major *c*-axis. Sometimes the magneto-crystalline anisotropy field may reorient this plane of magnetization without affecting the overall saturation magnetization and coercivity of that material [(Pullar, 2012), (Zhang *et al.*, 2014)]. The squareness ratio values (explain the anisotropy-dependent magnetic hardness of that system) are found to be within 0.2023 to 0.2622 and lie within the range of $0.05 < M_r/M_s < 0.5$. It implies that all these magnetic particles are of the pseudo-single domain in nature and coupled magneto-statically to each other [(Adeela *et al.*, 2016)]. The magnetic anisotropy values are found in good agreement with the coercivity (H_c). In consideration of the earlier reported studies, the substitution of Ti^{4+} ions with Fe^{3+} ions is expected to the overall decreasing behavior for magnetic anisotropy constant (K_1) [(Rao *et al.*, 2009),(Kąkol *et al.*, 1994)]. The only abnormalities associated with the sample x = 0.2 results may be due to the dependency of the magnetic anisotropy constant over the occupancy site and the discrete contribution of Fe^{2+} ions [(Kąkol *et al.*, 1994), (Fletcher and O'Reilly, 1974)]. The thermomagnetic analysis of all these hexaferrite samples confirms the existence of a sharp ferromagnetic (FM) to paramagnetic (PM) phase transition within it. This transition temperature is determined

with the help of a temperature-dependent first-order derivative (*dM/dT*) curve of magnetization. The presence of an intense downward peak is measured for the transition temperatures of each sample. The Curie temperature for the undoped Co_2-Y sample is found to be 603.76 K, which is in good agreement with the earlier reported value of 600 K by S.G. Lee *et al.* [(Lee and Kwon, 1996)]. This transition temperature shows a reverse trend with increasing the substitution of Ti^{4+} within the system. It can be explained based on the exchange interactions. The exchange interaction within the ferrite system decreases both magnetic ion density and overall magnetic moment value; hence lesser amount of thermal energy is required to surpass the weak exchange interaction of that sample. The substitution of diamagnetic Ti^{4+} ions replaces a magnetic ion Fe^{3+}, resulting in the lowering of exchange interactions within the system, and the Curie temperature shows a decreasing behavior [(Rao *et al.*, 2009)].

A diffuse reflectance-based-UV-visible spectrum is studied with all calcined powders to examine the optical characteristics (a crucial factor in designing photocatalysts). The as-obtained absorption spectra within a wavelength range of 200 to 1400 nm (displayed in Fig. 6.8) clearly signify the enhanced absorption of photons for titanium substituted samples as compared to the pure Co_2-Y sample. The bandgap energy (Eg) is the distance between the valance band (highest occupied orbit) and conduction band (lowest unoccupied orbit). This energy gap (Eg) can be measured either in terms of direct bandgap (measured vertical energy distance) or indirect bandgap (measured obliquely or inclined energy distance). To determine the energy band gap value (Eg) for all these hexaferrite samples, the Tauc relationship can be utilized as follows [(Mohammed *et al.*, 2021)]:

$$\frac{(\alpha.h_p.v)}{K_T} = \left(hv - E_g\right)^Q \qquad (6.1)$$

Here α is the coefficient of absorption, h_p represents the plank constant having a numerical value of 6.626 x 10^{-34} J.s, v is the incident photon frequency, K_T is an energy-independent

constant, and Q is dependent on the type of the transition such as 1/2 and 3/2 for allowed and forbidden direct transition, 2 and 3 for allowed and forbidden indirect transition [(Carol T *et al.*, 2022), (Naseri and Ghasemi, 2016)].

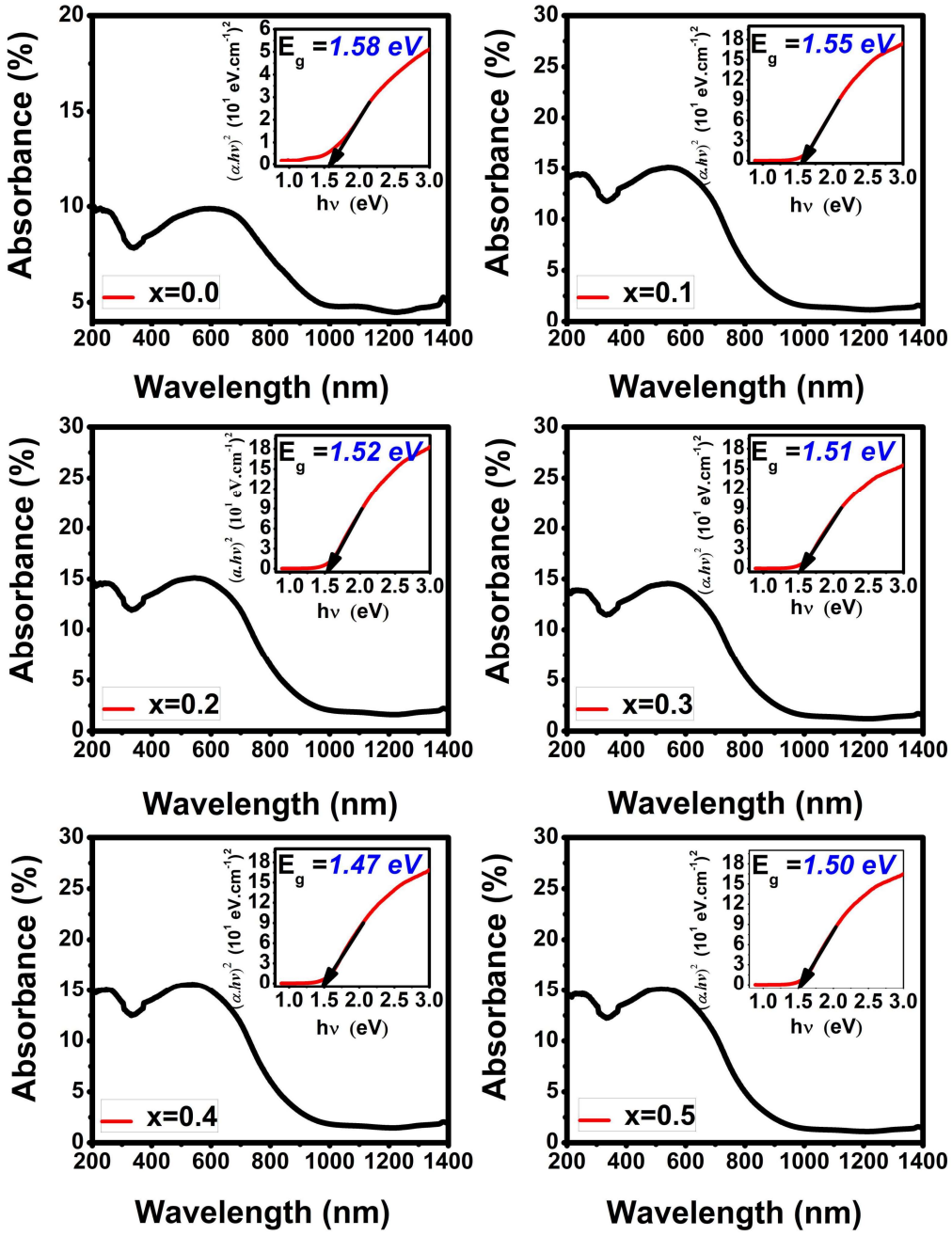

Figure. 6.8 UV-visible diffuse reflectance spectra along with Tauc plot for determination of direct band gap energy of calcined $Ba_2Co_2Fe_{12-x}Ti_xO_{22}$ (x = 0.0, 0.1, 0.2, 0.3, 0.4 & 0.5) ferrite powders.

. All these hexaferrite samples are investigated for their energy bandgap (E_g) value corresponding to the allowed direct transition with Q =1/2 using linear extrapolation to the graph between $(\alpha.h_p.v)^2$ and Eg; the obtained values are mentioned within the inset of Fig. 6.8. The results suggest that the bandgap energy is found to be decreased linearly with the substitution of Ti^{4+} ions. The decreasing order can be explained on behalf of structural defects and enhanced lattice distortions associated with the substitution of a larger cation into the hexaferrite system [(Mohammed *et al.*, 2021)]. It can also be associated with the increasing lattice parameter, which provides enhanced interatomic spacing, so the atoms can vibrate with large amplitude by utilizing thermal energy. This atomic vibration allows for lowering the electronic potential and lowering the energy bandgap [(Naseri and Ghasemi, 2016)]. The decreasing behavior of bandgap (E_g) can also be explained by the valency of both ions. Ti^{4+} ions have a higher valency state which substitutes for Fe^{3+} ions having a lower valency state. It generates impurity energy levels (donor type), which are responsible for the narrow bandgap [(Cai *et al.*, 2014)]. A slight enhancement of the bandgap (observed with x = 0.5) value can be explained by the dominance of the second factor, i.e., quantum confinement with decreasing particle size. The confinement of both electrons and holes within the nanoscale premises allows for the widening of the bandgap within semiconductors [(El-Hagary *et al.*, 2019),(Singh and Rajput, 2020)]. Due to enhanced photon absorption, along with the lowest bandgap energy (narrow bandgap results in the easy absorption of photon energy), two samples, $Ba_2Co_2Fe_{12}O_{22}$ (pristine Co_2-Y hexaferrite) and $Ba_2Co_2Fe_{11.6}Ti_{0.4}O_{22}$ (titanium substituted Co_2-Y hexaferrite), are studied for its comparative photocatalytic efficiency within the degradation of a non-biodegradable dye, i.e., methyl orange (MO).

The photocatalytic efficiency of $Ba_2Co_2Fe_{12}O_{22}$ and $Ba_2Co_2Fe_{11.6}Ti_{0.4}O_{22}$ ferrites are investigated for the degradation of methyl orange within an aqueous solution at room

temperature with a pH level of 3. The suitable selectivity of pH value decides the interaction between the catalyst and pollutant. The pH value of 3 is optimized by an earlier published study for the degradation of methyl orange within similar conditions [(De *et al.*, 2020)]. Fig. 6.9 shows the degradation process of aqueous methyl orange in both dark and visible light irradiation within the presence of H_2O_2. The result shows that there is no significant absorption loss within absorption spectra up to 50 minutes of test time, confirming the catalyst's necessity within the proposed scheme.

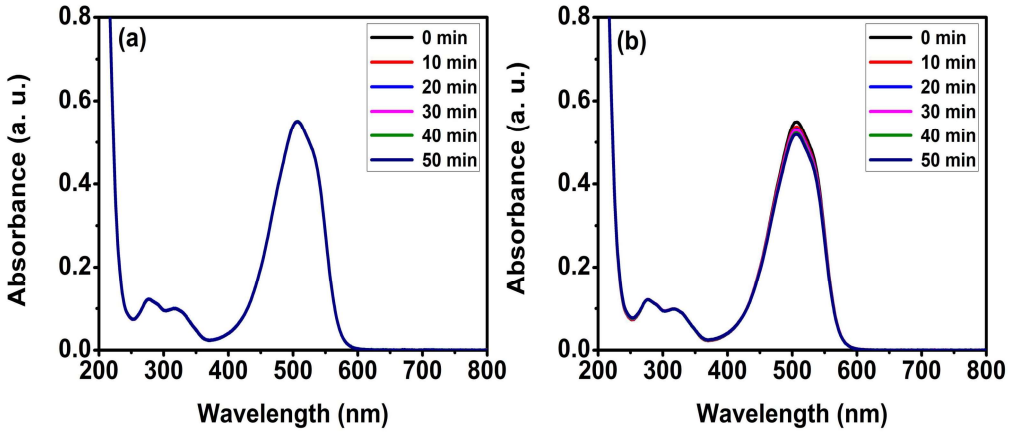

Figure 6.9 MO degradation in the absence of heterogeneous catalyst using H_2O_2 within (a) dark condition (Fenton) and (b) presence of visible light source (Photo-Fenton).

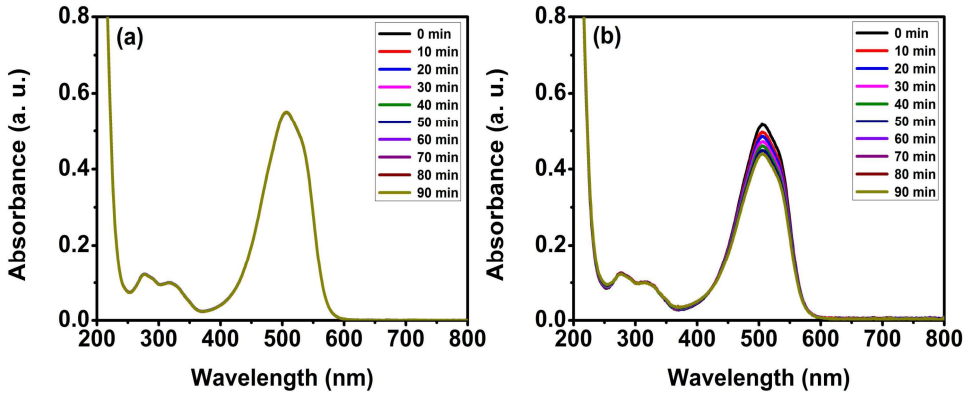

Figure 6.10 MO degradation with $Ba_2Co_2Fe_{12}O_{22}$ as a heterogeneous catalyst in the presence of H_2O_2 within (a) dark conditions (Fenton) and (b) presence of a visible light source (Photo-Fenton).

Fig. 6.10 shows the methyl orange (MO) degradation using $Ba_2Co_2Fe_{12}O_{22}$ as a heterogeneous catalyst in the presence of H_2O_2 within both dark (Fenton) and the presence of visible light source (Photo-Fenton). The result shows that the $Ba_2Co_2Fe_{12}O_{22}$ has poor degradation efficiency within the test time of 90 minutes, even in visible light irradiation.

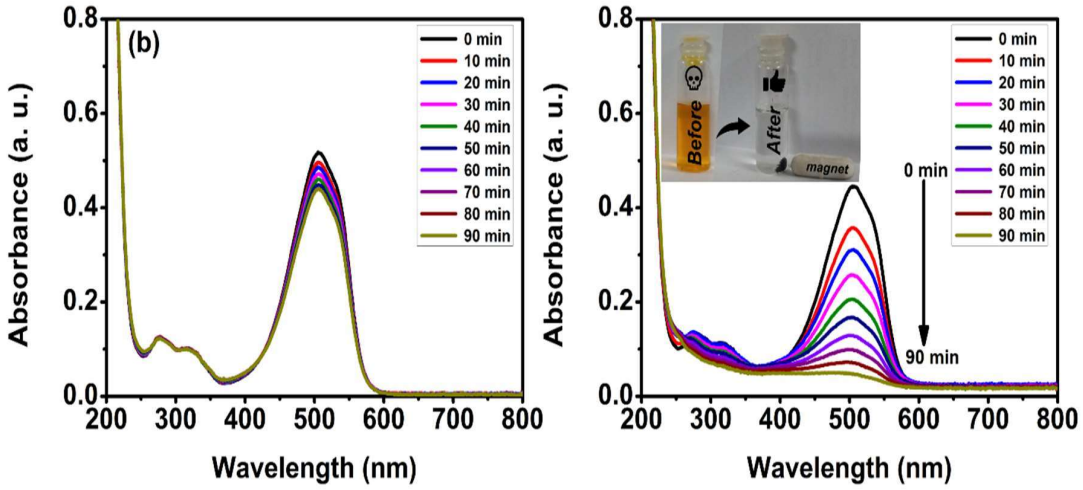

Figure 6.11 Role of titanium substitution in photocatalytic degradation of MO in the presence of both H_2O_2 and visible light source (Photo-Fenton) with (a) $Ba_2Co_2Fe_{12}O_{22}$ and (b) $Ba_2Co_2Fe_{11.6}Ti_{0.4}O_{22}$

The role of Ti^{4+} substitution over the degradation efficiency can be emphasized by analyzing both pristine and Ti^{4+} substituted samples for their dye degradation efficiency within similar conditions. The results (shown in Fig. 6.11) suggest that the $Ba_2Co_2Fe_{11.6}Ti_{0.4}O_{22}$ can efficiently degrade (nearly complete) the methyl orange (MO) within the test time of 90 minutes. The comparative performance of both these catalysts is analyzed based on the degradation rate for methyl orange, as shown in Fig. 6.12.(a). It describes the time-dependent variation of MO concentration at the time (C) with respect to the initial concentration (C_o), i.e., 4.6 mg/l. To quantify the performance of both these catalysts and determination of heterogeneously catalyzed kinetics of the MO

photodegradation, a standard Langmuir–Hinshelwood (L-H) equation is utilized with the following expression [(Almahri, 2022)].

$$ln\left(C/C_o\right) = -K_{arc}\,.\,t \qquad (6.2)$$

where K_{arc} is the apparent rate constant or pseudo-first-order rate constant. The rate constants (K_{arc}) are determined as the slope of $\ln(C/C_o)$ vs. time plots (shown in Fig. 6.12(b)). The rate constant values for $Ba_2Co_2Fe_{12}O_{22}$ and $Ba_2Co_2Fe_{11.6}Ti_{0.4}O_{22}$ are found to be 2.7 x 10^{-3} and 1.9 x 10^{-2} min^{-1}, respectively.

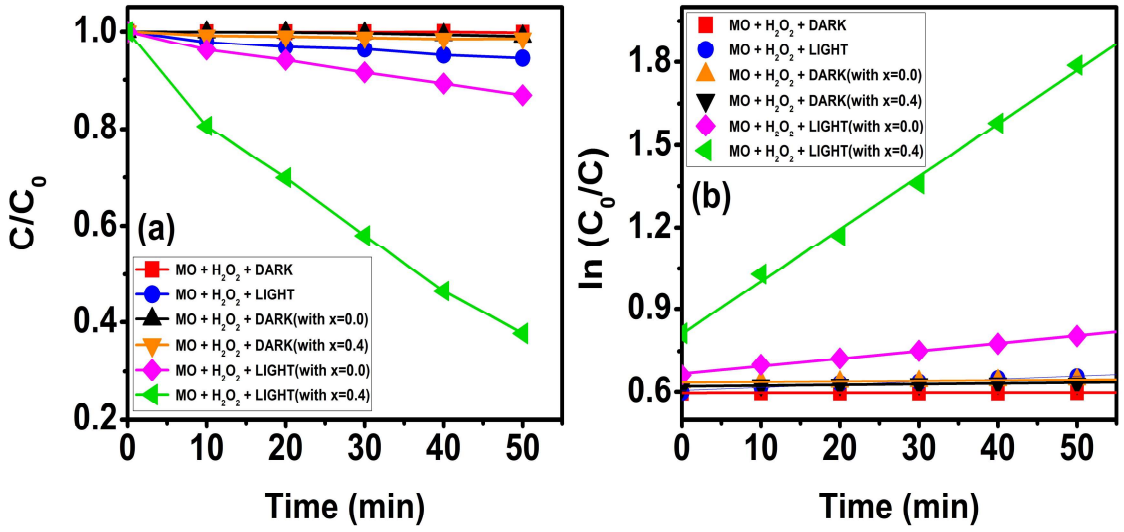

Figure 6.12 (a) Comparative analysis of MO degradation with $Ba_2Co_2Fe_{12}O_{22}$ and $Ba_2Co_2Fe_{11.6}Ti_{0.4}O_{22}$ under various controlled conditions (b) Comparison of first-order kinetics ($\ln(C_0/C)$ vs time plot) of both catalysts.

Another significant parameter, i.e., the turnover frequency (TOF), is also examined in these hexaferrite catalysts to compare the photocatalytic degradation performances within similar conditions. The turnover frequency is the number of reactants converted into a product within the presence of 1 g of heterogeneous catalyst in a unit of time [(Shang *et al.*, 2013)]. The turn over frequency values for $Ba_2Co_2Fe_{12}O_{22}$ and $Ba_2Co_2Fe_{11.6}Ti_{0.4}O_{22}$ are

found to be 7.49 x 10^{-7} and 3.93 x 10^{-6} mole $g^{-1}min^{-1}$, respectively. In a combined consideration of both the apparent rate constant (K_{arc}) and turnover frequency (TOF) values, the 0.1 mg of titanium substituted sample $Ba_2Co_2Fe_{11.6}Ti_{0.4}O_{22}$ shows the best performance with complete degradation of the methyl orange dye within 90 minutes at an initial concentration of 4.6 mg/l within the irradiation of visible light using a cool LED source giving an irradiance of 930 watts/m^2. This enrichment of catalytic activity can be correlated to various factors such as enhanced absorbance value, lowest band gap value, and fine particle size to facilitate the larger reactive sites.

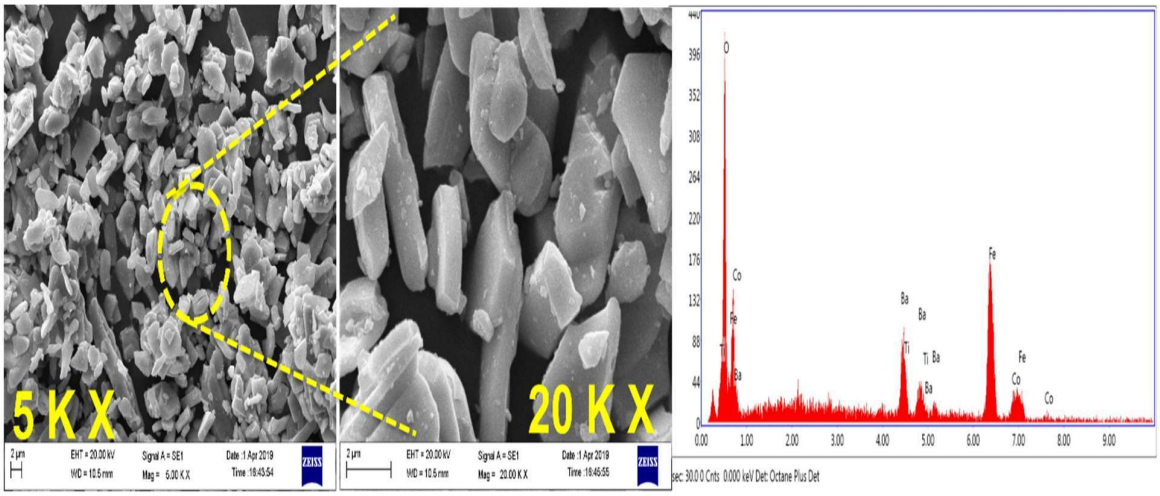

Figure 6.13 SEM micrographs of calcined $Ba_2Co_2Fe_{11.6}Ti_{0.4}O_{22}$ hexaferrite powder at two different magnifications of 5K and 20K, along with EDX analysis.

The surface morphological features of titanium substituted Co_2-Y hexaferrite ($Ba_2Co_2Fe_{11.6}Ti_{0.4}O_{22}$) are analyzed using scanning electron micrographs. Fig. 6.13 displays the micrographs of calcined powder at 5 K and 20 K magnifications along with corresponding EDX spectra, which confirms the elemental identity of this compound without any traces of impurity elements. The surface morphology reveals that the hexaferrite powder has a wide range of size distribution (from 0.15 µm to 3.61 µm) with an average particle size of 1.435 µm (standard deviation of 0.718), composed of the larger

hexagonal plate-like particle along with small particles (irregular shaped) distributed over the surface of these larger particles.

To validate the successful substitution of Ti^{4+} ions within the $Ba_2Co_2Fe_{11.6}Ti_{0.4}O_{22}$ hexaferrite sample, the electronic structures of all the elements are studied using XPS spectra recorded in the range of 1350 eV to 1 eV region. The relative contribution of each valance state is demonstrated qualitatively by deconvoluting the high-resolution X-ray photoelectron spectrum.

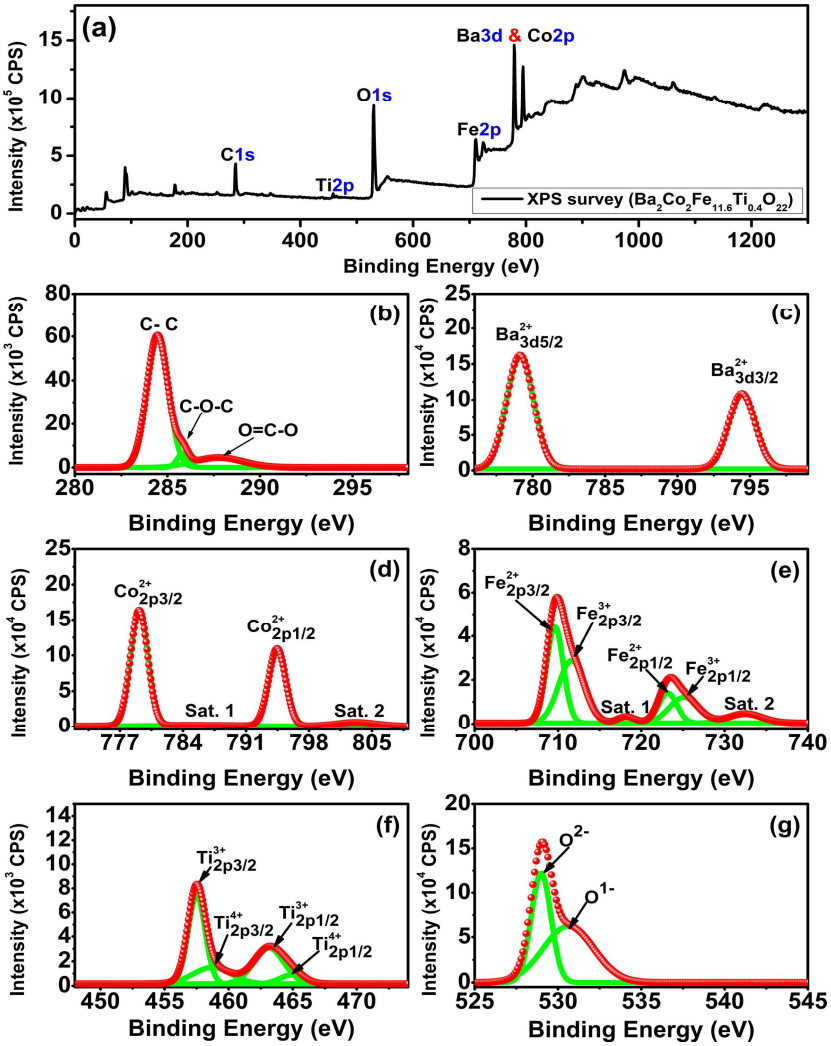

Figure 6.14 The XPS analysis of $Ba_2Co_2Fe_{11.6}Ti_{0.4}O_{22}$ hexaferrite (a) wide scan XPS survey and high-resolution core spectra of (b) C-1*s* (c) Ba-3*d* (d) Co-2*p* (e) Fe-2*p* (f) Ti-2*p*, and (g) O-1*s*.

A wide scan of XPS spectra, displayed in Fig. 6.14(a), validates the existence of Ba, Co, Fe, Ti, and O elements within it, without any impurity element except carbon. The respective C1*s* peak position (considered as an internal standard to calibrate the XPS data) is adjusted to 284.8 eV to compensate for the binding energies associated with all other peaks [(Suthar *et al.*, 2020), (Wu *et al.*, 2015)]. The high-resolution C1*s* spectra, displayed in Fig. 6.14(b), reveal the existence of three peaks (obtained through deconvolution of spectra) corresponding to the C-C bonding (284.80 eV), C-O-C bond (285.83 eV), O=C-O bond (287.76 eV), correspondingly [(Wu, Lin, and Xu, 2019)]. The high-resolution Ba-3*d* spectra, displayed in Fig. 6.14(c), confirm the existence of spin-orbit doublet for barium ions (Ba^{2+} state), consistent with Ba-3$d_{5/2}$ at 779.13 eV and Ba-3$d_{3/2}$ at 794.45 eV, having an energy interval of 15.32 eV [(Suthar *et al.*, 2020)]. The high-resolution Co-2*p* spectra, displayed in Fig. 6.14(d), confirm the existence of spin-orbit doublet for cobalt ions (Co^{2+} state), consistent with Co-2$p_{3/2}$ at 779.13 eV and Co-2$p_{1/2}$ at 794.46 eV having an energy interval of 15.33 eV along with two satellite peaks at 785.06 eV and 803.22 eV, correspondingly [(Suthar *et al.*, 2020)]. The high-resolution Fe-2*p* spectra, displayed within Fig. 6.14(e), confirm the existence of characteristic peaks for iron ions (mixed Fe^{3+} & Fe^{2+} states), consistent with Fe-2$p_{3/2}$ at 709.98 eV and Fe-2$p_{1/2}$ at 723.48 eV having an energy interval of 13.5 eV along with two satellite peaks at 718.20 eV and 732.47 eV, correspondingly. The further deconvolution of these two major characteristic peaks explains the co-existence of mixed valency states of iron ions within each orbit corresponding to Fe^{2+}-2$p_{3/2}$ at 709.50 eV, Fe^{2+}-2$p_{1/2}$ at 723.18 eV, Fe^{3+}-2$p_{3/2}$ at 711.62 eV and Fe^{3+}-2$p_{1/2}$ at 725.11 eV [(Suthar *et al.*, 2020)]. The high-resolution Ti-2*p* spectra, displayed within Fig. 6.14(f), confirm the existence of characteristic peaks for titanium ions (mixed Ti^{3+} & Ti^{4+} states), consistent with Ti-2$p_{3/2}$ at 457.48 eV and Ti-2$p_{1/2}$ at 463.28 eV having an energy interval of 5.8 eV. The further deconvolution of these two major

characteristic peaks explains the co-existence of mixed valency states of titanium ions within each orbit corresponding to Ti^{3+}-$2p_{3/2}$ at 457.50 eV, Ti^{3+}-$2p_{1/2}$ at 463.13 eV, Ti^{4+}-$2p_{3/2}$ at 458.70 eV and Ti^{4+}-$2p_{1/2}$ at 464.92 eV [(Woo *et al.*, 2020)]. The high-resolution O1*s* spectra, displayed within Fig. 6.14(g), reveal the existing two peaks (obtained through deconvolution of spectra) corresponding to the lattice oxygen or bonded oxygen (O^{2-}) at 528.98 eV and oxygen vacancy (O^{1-}) at 530.62 eV, correspondingly [(Suthar *et al.*, 2020)]. The XPS study confirms the mixed ionic states for iron ions (Fe^{2+} and Fe^{3+}) and titanium ions (Ti^{3+} and Ti^{4+}) within the sample. It may facilitate the electron transportation and enhanced redox configuration to the sample $Ba_2Co_2Fe_{11.6}Ti_{0.4}O_{22}$ [(Woo *et al.*, 2020)]. The existence of oxygen vacancy also helps to understand the enhanced photocatalytic activity. The presence of oxygen vacancy enhances the visible light absorption. It leads to narrowing the bandgap of the sample by generating an extra impurity level adjacent to the valence band [(Fernández-Climent, Giménez, and García-Tecedor, 2020),(Wang *et al.*, 2012)].

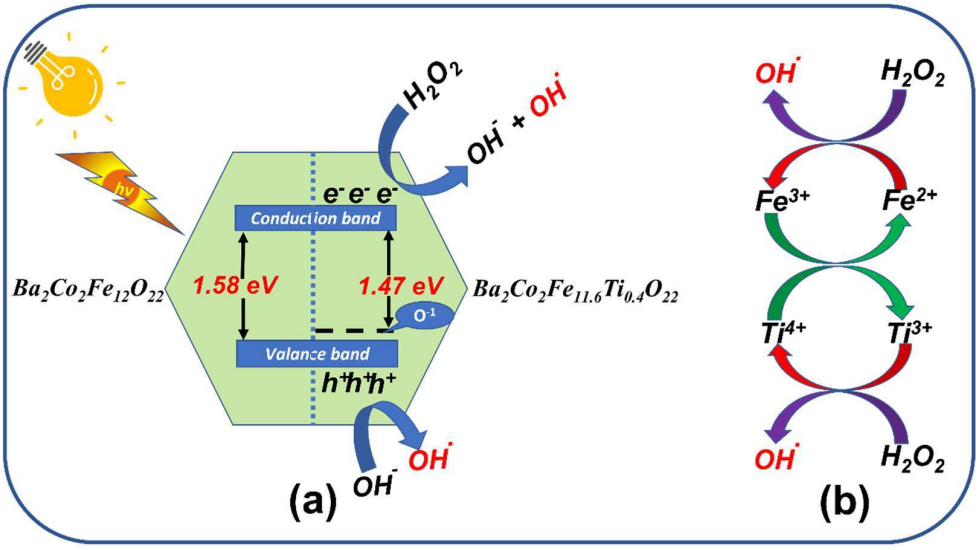

Figure 6.15 (a) Plausible mechanism for the generation of hydroxyl radicals ($OH^{\cdot}$) within the Photo-Fenton-based Co_2-Y type hexaferrite ferrite/H_2O_2 system. (b) generation of active hydroxyl radicals ($OH^{\cdot}$) by relocating electrons within the $Ba_2Co_2Fe_{11.6}Ti_{0.4}O_{22}$ hexaferrite system.

The $Ba_2Co_2Fe_{11.6}Ti_{0.4}O_{22}$ hexaferrite has a narrow bandgap value (E_g = 1.47 eV) as compared to the $Ba_2Co_2Fe_{12}O_{22}$ (E_g = 1.58 eV). It shows excellency within the photocatalytic degradation of methyl orange (MO). The degradation process (termed as Photo-Fenton type process) is performed under the presence of H_2O_2 (as a scavenger) and visible light irradiation, which degrades the MO from the wastewater by generating the active hydroxyl radicals ($OH^{\cdot}$). The admixture containing the hydrogen peroxide (H_2O_2) solution within transition metal cations (Fe^{3+}, Fe^{2+}, Ti^{4+}, Ti^{3+}) acts as a strong oxidant due to the greater oxidizing potential of generated hydroxyl radicals $OH^{\cdot}$ (2.84 V with respect to a standard hydrogen electrode (SHE)) [(Chahar *et al.*, 2021)]. The visible light plays a crucial role in this degradation process by generating photogenerated electron-hole pair by absorption of photon energy, and the electron moves from the valance band to the conduction band. These electron (e^-) and holes (h^+) are responsible for conducting redox reactions, resulting in the generation of hydroxyl radicals ($OH^{\cdot}$), as shown in Fig. 6.15(a). The generation of hydroxyl radicals ($OH^{\cdot}$) can also be understood with the electronic transition during the oxidation and reduction of transition metal cations, as shown in Fig. 6.15(b). The releasing electron with the oxidation of Ti^{3+} and Fe^{2+} is utilized to generate active hydroxyl radicals ($OH^{\cdot}$). The generation of these hydroxyl radicals ($OH^{\cdot}$) can be explained using the following steps [(Sharma, Bansal, and Singhal, 2015)]:

Step 1. Absorption of photon energy and generation of electron-hole pair

$$Ba_2Co_2Fe_{11.6}Ti_{0.4}O_{22} + h\nu \rightarrow Ba_2Co_2Fe_{11.6}Ti_{0.4}O_{22}(e^-_{C.B.} + h^+_{V.B.}) \quad (6.3)$$

Step 2. Utilization of photogenerated electrons ($e^-_{C.B.}$) by H_2O_2

$$H_2O_2 + e^-_{C.B.} \rightarrow OH^- + OH^{\cdot} \quad (6.4)$$

Step 3. Utilization of photogenerated hole ($h^+_{V.B.}$) by hydroxyl ion (OH^-)

$$OH^- + h^+_{V.B.} \rightarrow OH^{\cdot} \quad (6.5)$$

Step 4. The reaction of H_2O_2 with transition metal cations situated over the catalytic surface.

$$H_2O_2 + Fe^{3+} \rightarrow Fe^{2+} + H^+ + OOH\cdot \quad (6.6)$$

$$H_2O_2 + Fe^{2+} \rightarrow Fe^{3+} + OH^- + OH\cdot \quad (6.7)$$

$$H_2O_2 + Ti^{4+} \rightarrow Ti^{3+} + H^+ + OOH\cdot \quad (6.8)$$

$$H_2O_2 + Ti^{3+} \rightarrow Ti^{4+} + OH^- + OH\cdot \quad (6.9)$$

The hydroxyl radicals generated through these steps within the process degrade the methyl orange dye, as follows.

$$\text{MO} + H_2O_2(presence\ of\ Fe^{2+}, Ti^{3+}, Fe^{3+}, Ti^{4+}) \rightarrow Inorganic\ salt + CO_2 + H_2O \quad (6.10)$$

The overall degradation efficiency of $Ba_2Co_2Fe_{11.6}Ti_{0.4}O_{22}$ can be correlated with the facile generation of hydroxyl radicals ($OH^{\cdot}$) along with small crystallite size, presence of active Ti^{3+} species (promote the interaction of catalyst with reactants, retard the recombination of electron and hole) and Fe^{3+} & Fe^{2+} (responsible for trapping of electrons and holes, alter the recombination rate) [Khan and Swati, 2016].

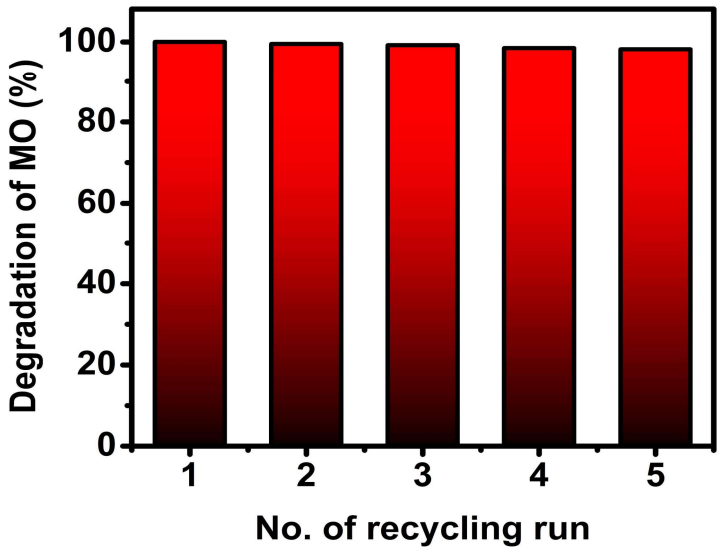

Figure 6.16 Reusability of the $Ba_2Co_2Fe_{11.6}Ti_{0.4}O_{22}$ hexaferrite as a catalyst for five consecutive recycling runs under similar conditions.

A better recyclability and chemical stability of any catalyst define its suitability to be adopted within large-scale processes. The re-processibility of the proposed catalyst ($Ba_2Co_2Fe_{11.6}Ti_{0.4}O_{22}$) is monitored for five consecutive runs after a facile magnetic separation, followed by washing with DI water and drying at 100°C. The recovered catalyst is again utilized for the same process to degrade the methyl orange from its aqueous solution, keeping all parameters similar as earlier. The results suggest no remarkable degradation efficiency loss (%), as shown in Fig. 6.16. It explains the better recyclability along with précised separation from the reaction product.

6.3 Summary

The single-phase pristine and Ti^{4+} substituted Y-type barium hexaferrite (Co_2-Y) having a general formula of {$Ba_2Co_2Fe_{12-x}Ti_xO_{22}$ (x = 0.0, 0.1, 0.2, 0.3, 0.4 & 0.5)} are successfully prepared using the nitrate-based sol-gel auto-combustion route. The as-prepared Co_2-Y hexaferrite powders have robust thermo-chemical stability, which can overcome the problem associated with spinel-based ferrites. The structural investigations using XRD and FTIR confirm the successful substitution of titanium ions within the hexaferrite system. The magnetic studies confirm the presence of ferrimagnetic nature within all samples. The UV-visible spectrum analysis supports the enhancement in visible light absorption and decreasing behavior for bandgap value by increasing the substitution level of Ti^{4+} ions within the sample. The photocatalytic degradation study of aqueous MO solution in the presence of H_2O_2 suggests the superiority of $Ba_2Co_2Fe_{11.6}Ti_{0.4}O_{22}$ compared to pristine Co_2-Y barium hexaferrite with an apparent rate constant of 1.9 x 10^{-2} min^{-1} and turn over frequency of 3.93 x 10^{-6} mole $g^{-1}min^{-1}$. This enhanced photocatalytic activity for sample $Ba_2Co_2Fe_{11.6}Ti_{0.4}O_{22}$ can be correlated to the fine crystallite size; the presence of active Ti^{3+} species to promote the reactivity of catalyst surface; the presence of mixed Fe^{3+}

& Fe^{2+} to slow down the recombination process by trapping the photogenerated electrons and holes; the existence of oxygen vacancy to enhance the visible light absorption and leads to narrowing the bandgap by creating an extra impurity level adjacent to the valence band. The results suggest that the $Ba_2Co_2Fe_{11.6}Ti_{0.4}O_{22}$ ferrite can be utilized as a promising material (facile synthesis, enhanced thermal and chemical stability, enhanced apparent rate constant value) to catalyze the degradation of several non-biodegradable organic compounds from wastewater in large-scale industries, without any hazardous footprint on the environment.